

## ARTICLES

# A synchronized quorum of genetic clocks

Tal Danino<sup>1\*</sup>, Octavio Mondragón-Palomino<sup>1\*</sup>, Lev Tsimring<sup>2</sup> & Jeff Hasty<sup>1,2,3</sup>

The engineering of genetic circuits with predictive functionality in living cells represents a defining focus of the expanding field of synthetic biology. This focus was elegantly set in motion a decade ago with the design and construction of a genetic toggle switch and an oscillator, with subsequent highlights that have included circuits capable of pattern generation, noise shaping, edge detection and event counting. Here we describe an engineered gene network with global intercellular coupling that is capable of generating synchronized oscillations in a growing population of cells. Using microfluidic devices tailored for cellular populations at differing length scales, we investigate the collective synchronization properties along with spatiotemporal waves occurring at millimetre scales. We use computational modelling to describe quantitatively the observed dependence of the period and amplitude of the bulk oscillations on the flow rate. The synchronized genetic clock sets the stage for the use of microbes in the creation of a macroscopic biosensor with an oscillatory output. Furthermore, it provides a specific model system for the generation of a mechanistic description of emergent coordinated behaviour at the colony level.

Synchronized clocks are of fundamental importance in the coordination of rhythmic behaviour among individual elements in a community or a large complex system. In physics and engineering, the Huygens paradigm of coupled pendulum clocks<sup>1–3</sup> has permeated diverse areas from the development of arrays of lasers<sup>4</sup> and superconducting junctions<sup>5</sup> to Global Positioning System (GPS)<sup>6</sup> and distributed sensor networks<sup>7</sup>. In biology, a vast range of intercellular coupling mechanisms lead to synchronized oscillators that govern fundamental physiological processes, such as somitogenesis, cardiac function, respiration, insulin secretion and circadian rhythms<sup>8–15</sup>. Typically, synchronization helps stabilize a desired behaviour arising from a network of intrinsically noisy and unreliable elements. Sometimes, however, the synchronization of oscillations can lead to severe malfunction of a biological system, as in epileptic seizures<sup>16</sup>.

There is considerable interest in the use of synthetic biology to recreate complex cellular behaviour from the underlying biochemical reactions that govern gene regulation and signalling. Synthetic biology can be broadly parsed into efforts aimed at the large-scale synthesis of DNA and the forward engineering of genetic circuits from known biological components. In the area of DNA synthesis, pathways have been perturbed and replaced<sup>17</sup> in an effort to understand the network motifs and transcriptional regulatory mechanisms that control cellular processes and elicit phenotypic responses<sup>18</sup>. On a larger scale, progress has been made towards the creation of entire genomes, providing new insights into what constitutes the minimal set of genes required for microbial life<sup>19</sup>.

The genetic circuits approach to synthetic biology involves the forward engineering of relatively small gene networks using computational modelling<sup>20,21</sup>. Here, the original toggle switch<sup>22</sup> and oscillator<sup>23</sup> have inspired the design and construction of circuits capable of controlling cellular population growth<sup>24</sup>, generating specific patterns<sup>25</sup>, triggering biofilm development<sup>26</sup>, shaping intracellular noise<sup>27</sup>, detecting edges in an image<sup>28</sup>, and counting discrete cellular events<sup>29</sup>. In the context of rhythmic behaviour, there have been recent successes in the construction of intracellular oscillators that mimic naturally occurring clocks<sup>30–33</sup>. As well as their potential as biological sensors, these clock networks have led to insights about the functionality of

circadian networks<sup>34</sup>. A unifying theme for most of the genetic circuit studies is a particular focus on dynamical behaviour. Thus, the circuits are constructed and monitored in single cells, typically with fluorescent reporters, and new measurement technologies are often developed in parallel<sup>35</sup>. Furthermore, because nonlinearities and stochasticity arise naturally, tools from the fields of nonlinear dynamics and statistical physics are extremely useful both in the generation of design specifications and for careful comparison between experiment and computational model.

## Synchronized genetic oscillators

The synchronized oscillator design (Fig. 1a) is based on elements of the quorum sensing machineries in *Vibrio fischeri* and *Bacillus Thuringensis*. We placed the *luxI* (from *V. fischeri*), *aiiA* (from *B. Thuringensis*) and *yemGFP* genes under the control of three identical copies of the *luxI* promoter. The LuxI synthase enzymatically produces an acyl-homoserine lactone (AHL), which is a small molecule that can diffuse across the cell membrane and mediates intercellular coupling. It binds intracellularly to the constitutively produced LuxR, and the LuxR–AHL complex is a transcriptional activator for the *luxI* promoter<sup>36</sup>. *AiiA* negatively regulates the promoter by catalysing the degradation of AHL<sup>37</sup>. This network architecture, whereby an activator activates its own protease or repressor, is similar to the motif used in other synthetic oscillator designs<sup>30–32</sup> and forms the core regulatory module for many circadian clock networks<sup>13,38,39</sup>. Furthermore, theoretical work has shown how the introduction of an autoinducer in similar designs can potentially lead to synchronized oscillations over a population of cells<sup>40,41</sup>.

Most quorum sensing systems require a critical cell density for generation of coordinated behaviour<sup>42</sup>. We modified the local cell density of the synchronized oscillator cells (denoted TDQS1) through the use of microfluidic devices<sup>35,43</sup> of differing geometries. The device used for monitoring the bulk oscillations consists of a main nutrient-delivery channel that feeds a rectangular trapping chamber (Fig. 1b). Once seeded, a monolayer of *Escherichia coli* cells grow in the chamber and cells are eventually pushed into the channel where they then flow to the waste port. This device allows for a constant supply of nutrients

<sup>1</sup>Department of Bioengineering, <sup>2</sup>BioCircuits Institute, University of California, San Diego, La Jolla, California 92093, USA. <sup>3</sup>Molecular Biology Section, Division of Biological Science, University of California, Mailcode 0368, La Jolla, California 92093, USA.

\*These authors contributed equally to this work.

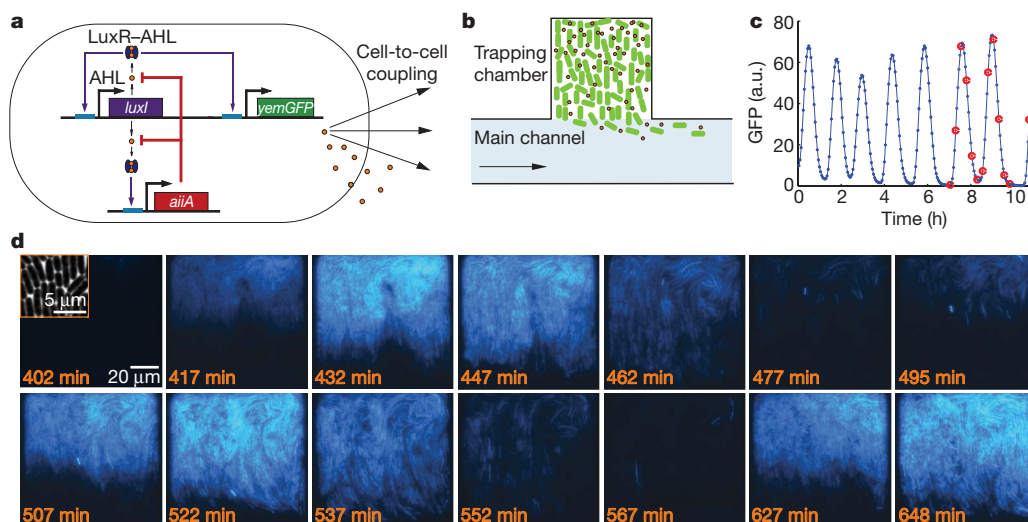


**Figure 1 | Synchronized genetic clocks.** **a**, Network diagram. The *luxI* promoter drives production of the *luxI*, *aiiA* and *yemGFP* genes in three identical transcriptional modules. LuxI enzymatically produces a small molecule AHL, which can diffuse outside of the cell membrane and into neighbouring cells, activating the *luxI* promoter. AiiA negatively regulates the circuit by acting as an effective protease for AHL. **b**, Microfluidic device used for maintaining *E. coli* at a constant density. The main channel supplies media to cells in the trapping chamber, and the flow rate can be externally

or inducers and the maintenance of an exponentially growing colony of cells for more than 4 days. We found that chamber sizes of  $100 \times (80\text{--}100) \mu\text{m}^2$  were ideal for monitoring the intercellular oscillator, as they allowed for sufficient nutrient distribution and optimal cell and AHL densities. In the context of the design parameters, the flow rate can be modulated to change the local concentration of AHL. Furthermore, the device can be modified to permit the observation of spatial waves over longer length scales.

After an initial transient period, the TDQS1 cells exhibit stable synchronized oscillations that are easily discernible at the colony level (Fig. 1c, d and Supplementary Movies 1–2). The dynamics of the oscillations can be understood as follows. Because AHL is swept away by the fluid flow and is degraded by AiiA internally, a small colony of individual cells cannot produce enough inducer to activate expression from the *luxI* promoter. However, once the population reaches a critical density, there is a ‘burst’ of transcription of the *luxI* promoters, resulting in increased levels of LuxI, AiiA and green fluorescent protein (GFP). As AiiA accumulates, it begins to degrade AHL, and after a sufficient time, the promoters return to their inactivated state. The production of AiiA is then attenuated, which permits another round of AHL accumulation and another burst of the promoters.

To determine how the effective AHL dissipation rate affects the period of the oscillations, we conducted a series of experiments at various channel flow rates. At high flow rate, the oscillations stabilize after an initial transient and exhibit a mean period of  $90 \pm 6$  min and mean amplitude of  $54 \pm 6$  GFP arbitrary units (Fig. 2a and Supplementary Movie 2). At low flow rate, we observed a period of  $55 \pm 6$  min and amplitude of  $30 \pm 9$  GFP arbitrary units. Notably, the waveforms have differing shape, with the slower oscillator reaching a trough near zero after activation, and the faster oscillator decaying to levels above the original baseline (Fig. 2b). We swept the flow rate from  $180$  to  $296 \mu\text{m min}^{-1}$  and observed an oscillatory period from 52–90 min (Fig. 2c). Moreover, we found the amplitude to be proportional to the period of the oscillations (Fig. 2d), which is consistent with ‘degrade-and-fire’ oscillations<sup>44</sup> observed in a previously reported intracellular oscillator<sup>31</sup>.

### Spatiotemporal dynamics

In experiments conducted at low flow rate, we observed the spatial propagation of the fluorescence signal across the 100- $\mu\text{m}$  chamber.

controlled to change the effective degradation rate of AHL. **c**, Bulk fluorescence as a function of time for a typical experiment in the microfluidic device. The red circles correspond to the image slices in **d**. a.u., arbitrary units. **d**, Fluorescence slices of a typical experimental run demonstrate synchronization of oscillations in a population of *E. coli* residing in the microfluidic device (Supplementary Movie 1). Inset in the first snapshot is a  $\times 100$  magnification of cells.

To investigate these spatiotemporal dynamics in more detail, we redesigned the microfluidic chip with an extended 2-mm trapping chamber (Supplementary Information). Snapshots of a typical experimental run are presented in Fig. 3a (Supplementary Movies 3 and 4). A few isolated colonies begin to grow and subsequently merge into a large monolayer that fills the chamber (Fig. 3a, 66 min). At 100 min, there is a localized burst of fluorescence that propagates to the left and right in subsequent frames (Fig. 3a, 100–118 min). A second burst occurs near the original location and begins to propagate to the left and right as before.

To illustrate the spatiotemporal information contained in an entire 460-min image sequence, we plot the fluorescence intensity as a function of time and distance along the chamber (Fig. 3b). Note

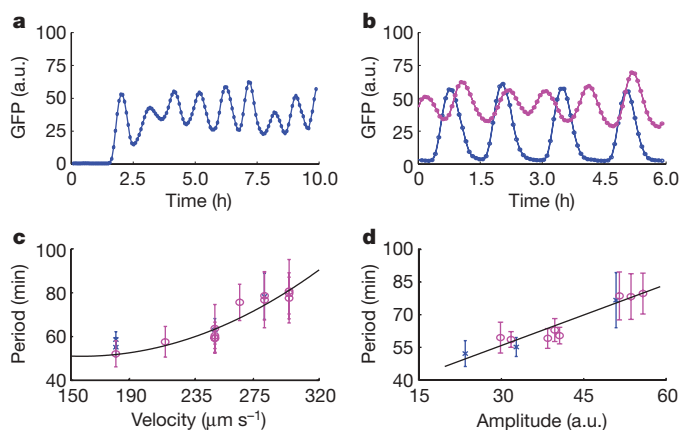


**Figure 2 | Dynamics of the synchronized oscillator under several microfluidic flow conditions.** (See also Supplementary Movies 1 and 2.) **a**, At around 90 min, cells begin to oscillate synchronously after reaching a critical density in the trap. **b**, The period and amplitude increase for higher flow rates. Magenta curve is at low velocity ( $240 \mu\text{m min}^{-1}$ ), blue is at higher velocity ( $280 \mu\text{m min}^{-1}$ ). **c**, Period as a function of velocity in the main channel showing tunability of period between 55–90 min. **d**, Period versus amplitude for all experiments. Magenta circles (**c**, **d**) are data from 84 and  $90 \mu\text{m}$  traps, blue crosses are  $100 \mu\text{m}$  traps. Error bars in **c** and **d** indicate  $\pm 1$  s.d. for a single channel, averaged over 10–50 peaks; each data point represents a different run.

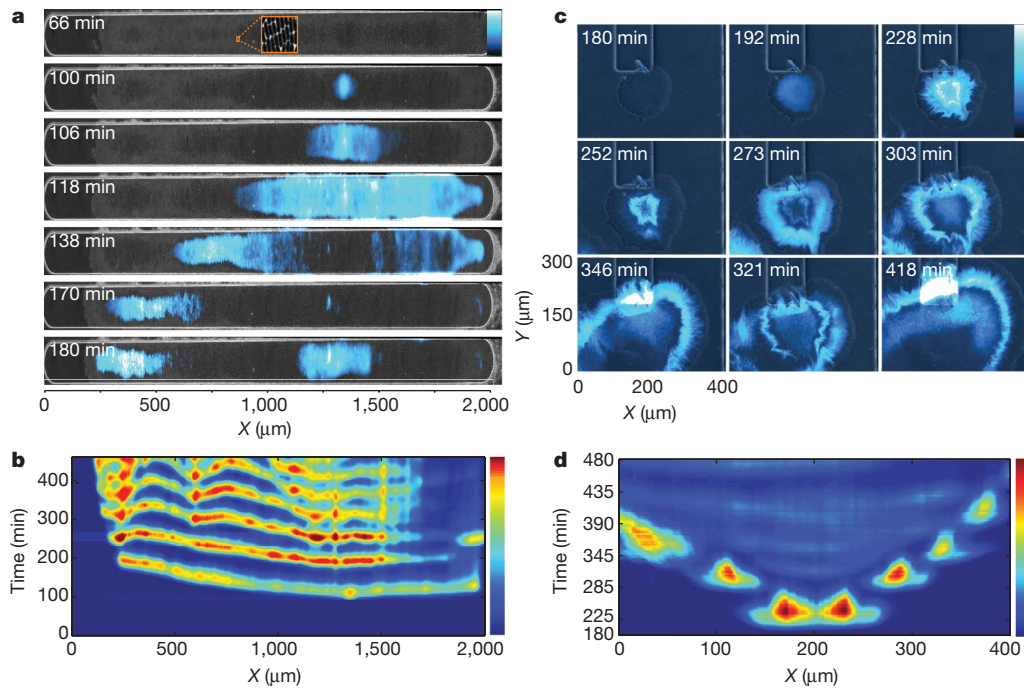


**Figure 3 | Spatiotemporal dynamics of the synchronized oscillators.**

**a**, Snapshots of the GFP fluorescence superimposed over brightfield images of a densely packed monolayer of *E. coli* cells are shown at different times after loading (Supplementary Movies 3 and 4). Travelling waves emerge spontaneously in the middle of the colony and propagate outwards with a speed of  $\sim 8\text{--}35\ \mu\text{m}\ \text{min}^{-1}$ . At later times waves partially lose coherence owing to inhomogeneity in cell population and intrinsic instability of wave propagation. **b**, Corresponding space–time diagram showing the

the correspondence of this space–time plot to the images in Fig. 3a. During the first 100 min, there is no activity and the space–time plot is blue, indicating no fluorescence. Then at 100 min, there is an orange spot at around  $1,350\ \mu\text{m}$ , corresponding to the burst in Fig. 3a. In the space–time plot, propagation of a wave to the left and right appears as a green–yellow concave line. The larger slope to the left of the burst origin indicates that the leftward moving wave is travelling slower ( $\sim 25\ \mu\text{m}\ \text{min}^{-1}$ ) than the rightward wave ( $\sim 35\ \mu\text{m}\ \text{min}^{-1}$ ). Subsequent waves originating from a nearby location arise as further orange–yellow intensity lines. These intensity lines indicate ‘annihilation events’, where leftward moving and rightward moving waves collide and annihilate each other. Although these events are prominent in the movies (Supplementary Movies 3 and 4) they appear subtly in the space–time plot at locations where positive and negative slopes meet ( $300\text{--}400\ \mu\text{m}$  in second intensity line and on). As the travelling wave gets further from a burst location it breaks off into a packet (170 min) that travels leftward at  $12.5\ \mu\text{m}\ \text{min}^{-1}$  initially, and slows to  $8.5\ \mu\text{m}\ \text{min}^{-1}$  towards the end of the trap where the cell density is lower (between 118–200 min). The corresponding cell–density space–time plot shows that a higher density of cells is first reached at the centre of the colony and is minimal towards the left-moving edge (Supplementary Fig. 3 and Supplementary Movie 3). As a result, the critical cell and AHL densities for wave propagation are reached at different times and spatial locations.

We also investigated how the intercellular oscillator behaves in a three-dimensional colony growing in a  $400 \times 1,000 \times 4.0\ \mu\text{m}^3$  microfluidic chamber (Fig. 3c, d and Supplementary Movie 5). In this device, the colony grows radially over the course of 180 min without fluorescing until it reaches a size of approximately  $100\ \mu\text{m}$ . At this time, a large fluorescence burst originates from the centre of the colony, with a bright band near the centre (Fig. 3c, 228 min). During this first burst (273 min), the bright band shows that cells at an intermediate cell density have a larger amplitude and longer period than cells near the front or in the interior. As the colony

fluorescence of cells along the centre of the trap as a function of time.

**c**, Snapshots of the GFP fluorescence superimposed over the brightfield images of a three-dimensional growing colony of *E. coli* cells at different times after loading (Supplementary Movie 5). Bursts of fluorescence begin when the growing colony reaches a critical size of about  $100\ \mu\text{m}$ . These bursts are primarily localized at the periphery of the growing colony.

**d**, Corresponding space–time diagram showing fluorescence of cells along a horizontal line through the centre of the growing colony.

expands a further  $50\text{--}100\ \mu\text{m}$  in diameter, a second burst of fluorescence occurs at a similar intermediate cell density. Subsequent oscillations are seen as the cell growth front propagates, whereas weak oscillations arise and quickly die inside the colony.

### Quantitative modelling

To describe quantitatively the mechanisms driving bulk synchronization and wave propagation, we developed a computational model using delayed differential equations for protein and AHL concentrations (Supplementary Information). Although conceptually the nature of oscillations is reminiscent of the degrade-and-fire oscillations observed in a dual delayed feedback circuit<sup>31,44</sup>, an important difference is the coupling among genetic clocks in different cells through extracellular AHL. The modelling of this coupling, and the related cell-density dependence, allowed us to explain most of the non-trivial phenomenology of the spatiotemporal quorum clock dynamics.

A broad range of model parameters lead to oscillations (Fig. 4a–d), although there is a distinct absence of oscillations at small and large cell densities for low to medium flow values (Fig. 4c). The qualitative nature of the oscillations can be explained using Fig. 4a. Each period begins with the latent accumulation of both AiiA and LuxI, which after a delay burst rapidly to high values. That burst suppresses AHL and further production of AiiA and LuxI. Both of these proteins then decay enzymatically, after which the process repeats. As expected, the period of the oscillations is roughly proportional to the enzymatic protein decay time. The period grows with the external AHL flow rate (effective degradation) and the amplitude of the oscillations, in good agreement with the experiments (compare Fig. 4b with Fig. 3c, d).

We modelled the collective spatiotemporal dynamics of the clocks by generalizing the bulk model to include the coupling of individual oscillators through extracellular AHL. The model consists of a one-dimensional array of ‘cells’, each of which is described by the same set of delay-differential equations coupled to a common, spatially

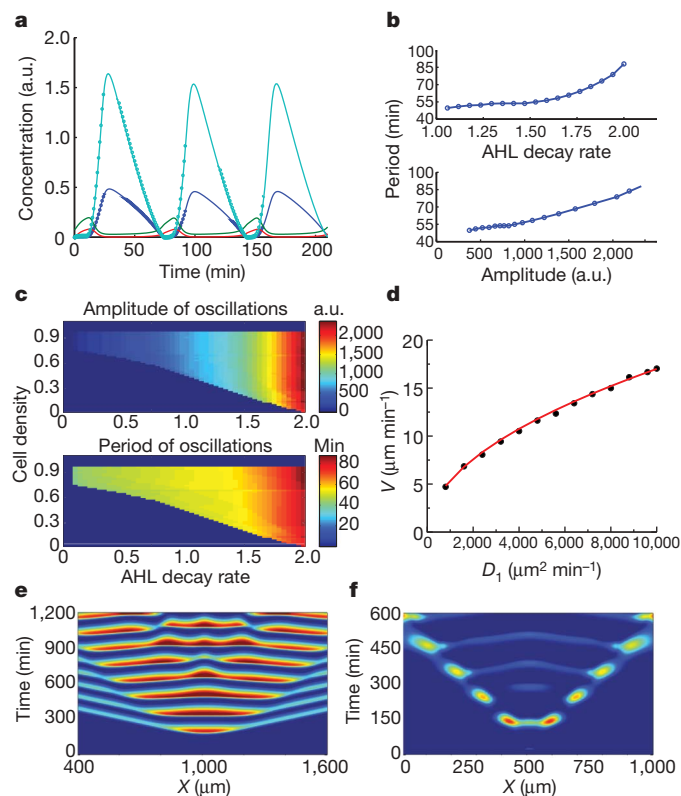


**Figure 4 | Modelling of synchronized genetic clocks.** **a**, A typical time series of concentrations of LuxI (cyan circles), AiiA (blue circles), internal AHL (green line) and external AHL (red line). LuxI and AiiA closely track each other, and are anti-phase with the concentrations of external and internal AHL. **b**, Period of oscillations as a function of the flow rate  $\mu$  at cell density  $d = 0.5$  (top). Period as a function of the amplitude of oscillations for the same cell density (bottom). **c**, Period and amplitude as a function of cell density and AHL decay rate  $\mu$ . Oscillations occur over a finite range of cell densities, and period increases with  $\mu$  after the bifurcation line is crossed. The results in **c** and **d** compare favourably with the experimental results in Fig. 2c, d. **d**, Speed of wave front propagation as a function of the diffusion coefficient  $D_1$ . The numerical data scale as  $V \sim D_1^{1/2}$  (red line). **e**, Space–time diagram of travelling waves propagating through a uniform array of cells corresponding to the experiment depicted in Fig. 3a, b. **f**, Space–time diagram of bursting oscillations in a growing cell population corresponding to the experiments in Fig. 3c, d.

non-uniform field of extracellular AHL. The latter is described by a linear diffusion equation with sources and sinks owing to AHL diffusion through the cell membrane and dilution. A small AHL perturbation in the middle of the array initiates waves of LuxI concentration (Fig. 4e), in excellent agreement with the experimental findings (compare Figs 3b and 4e). The velocity of the front propagation depends on the external AHL diffusion coefficient  $D_1$  (Fig. 4d and Supplementary Information), and for experimentally relevant values of  $D_1$ , the simulated front velocity is in good agreement with experimental data. Furthermore, cell density has an important role in wave propagation. To model the evolution of the three-dimensional colony (Fig. 3c, d), we set the functional form of the cell density to be an expanding ‘Mexican hat’, as observed in the experiments. Oscillations are then suppressed by the high density of cells in the middle of the colony, and LuxI bursts only occur on the periphery of the growing colony of cells. This phenomenology is also in excellent agreement with our experimental findings (compare Figs 4f and 3d).

## Emergence

On a fundamental level, the synchronized oscillations represent an emergent property of the colony that can be mechanistically explained in terms of the circuit design. Oscillations arise because

the small molecule AHL has a dual role, both enabling activation of the genes necessary for intracellular oscillations and mediating the coupling between cells. Because unbounded growth of the colony leads to an accumulation of AHL that ultimately quenches the bulk oscillations, we used open-flow microfluidic devices to allow for the flow of AHL away from the colony. At low cell densities, oscillations do not occur, because intracellular gene activation is decreased as AHL diffuses across the cell membrane and out of the chamber. At intermediate cell densities (that is, a full chamber), the increased production of AHL in each cell acts to mitigate the outward flow such that activation of the genes can occur in a rhythmic fashion, and colony-wide oscillations emerge in a seemingly spontaneous manner.

A natural question arises about the behaviour of individual cells in the absence of coupling. Although experimentally we cannot turn off the coupling while maintaining intracellular gene activation, we addressed this question using simulations by artificially setting the AHL diffusion rate across the cell membrane to zero (with the other parameters fixed). We find that individual cells oscillate independently for any cell density because they are completely decoupled from the environment and each other. This result indicates that the coupling through AHL diffusion provides a means for the synchronization of individual oscillators at intermediate cellular concentrations.

## Perspective and outlook

In the mid-seventeenth century, Christiaan Huygens serendipitously observed that two pendulum clocks oscillated in synchrony when mounted to a common support beam<sup>1</sup>. Although observations of synchronization in nature surely predate the age of enlightenment, Huygens is credited as the first to systematically characterize the synchronization of oscillators in terms of a known coupling mechanism (which, in the case of the pendula, he deduced as vibrations in the common support). We have shown how quorum sensing can be used to couple genetic clocks, leading to synchronized oscillations at the colony level. Given the single-cell variability and intrinsic stochasticity of most synthetic gene networks<sup>27,30,31,45,46</sup>, the use of quorum sensing is a promising approach to increasing the sensitivity and robustness of the dynamic response to external signals. Along these lines, our results set the stage for the design of networks that can function as spatially distributed sensors or synthetic machinery for coupling complex dynamical processes across a multicellular population.

## METHODS SUMMARY

**Strains, growth conditions.** Three identical transcriptional cassettes for *luxI*, *aiiA* and *yemGFP* were constructed by replacing the promoter of a modular pZ plasmid<sup>47</sup> (with *yemGFP*) with the *lux* operon from the native *V. fischeri* operon (*luxR* up to *luxI* stop codon)<sup>48</sup>. *luxI* and *aiiA*<sup>49</sup> genes were cloned in place of *yemGFP*, and a degradation tag was added to the carboxy-terminal of each. A previously used MG1655 strain of *E. coli*<sup>1</sup> was transformed with plasmids pTD103luxI/GFP(*colE1*,Kan) and pTD103aiiA(*p15A*,Amp) to create strain TDQS1 (Supplementary Information).

Each experiment started with a 1:1,000 dilution of overnight culture grown in 50 ml LB (10 g l<sup>-1</sup> NaCl) with antibiotics 100  $\mu$ g ml<sup>-1</sup> ampicillin (Amp) and 50  $\mu$ g ml<sup>-1</sup> kanamycin (Kan) for approximately 2 h. Cells reached an  $A_{600\text{ nm}}$  of 0.05–0.1, and were spun down and concentrated in 5 ml of fresh media with surfactant concentration of 0.075% Tween20 (Sigma-Aldrich) before loading in a device.

**Microfluidics and microscopy.** Images were acquired using an epifluorescent inverted microscope (TE2000-U, Nikon Instruments Inc.), and chip temperatures were maintained at 37 °C with a plexiglass incubation chamber encompassing the entire microscope. Phase-contrast and fluorescent images were taken at  $\times 20$  or  $\times 60$  every 2–5 min, and focus was maintained automatically using Nikon Elements software.

Received 20 August; accepted 4 December 2009.

- Huygens, C. *Œuvres complètes de Christiaan Huygens* Vol. 17 (Martinus Nijhoff, The Hague, 1932).
- Pikovsky, A., Rosenblum, M. & Kurths, J. *Synchronization: A Universal Concept in Nonlinear Sciences* (Cambridge, 2001).
- Strogatz, S. *Sync* (Penguin Books New York, 2004).

4. Vladimirov, A. G., Kozyreff, G. & Mandel, P. Synchronization of weakly stable oscillators and semiconductor laser arrays. *Europhys. Lett.* **61**, 613–619 (2003).
5. Wiesenfeld, K., Colet, P. & Strogatz, S. Synchronization transitions in a disordered Josephson series array. *Phys. Rev. Lett.* **76**, 404–407 (1996).
6. Lewandowski, W., Azoubib, J. & Klepczynski, W. GPS: primary tool for time transfer. *Proc. IEEE* **87**, 163–172 (1999).
7. Li, D., Wong, K., Hu, Y. & Sayeed, A. Detection, classification and tracking of targets in distributed sensor networks. *IEEE Signal Process. Mag.* **19**, 17–29 (2002).
8. Winfree, A. T. Biological rhythms and the behavior of populations of coupled oscillators. *J. Theor. Biol.* **16**, 15–42 (1967).
9. Mirollo, R. & Strogatz, S. Synchronization of pulse-coupled biological oscillators. *SIAM J. Appl. Math.* **50**, 1645–1662 (1990).
10. Elson, R. C. et al. Synchronous behavior of two coupled biological neurons. *Phys. Rev. Lett.* **81**, 5692–5695 (1998).
11. Jiang, Y.-J. et al. Notch signalling and the synchronization of the somite segmentation clock. *Nature* **408**, 475–479 (2000).
12. Glass, L. Synchronization and rhythmic processes in physiology. *Nature* **410**, 277–284 (2001).
13. Young, M. W. & Kay, S. Time zones: a comparative genetics of circadian clocks. *Nature Rev. Genet.* **2**, 702–715 (2001).
14. Chabot, J. R., Pedraza, J., Luitel, P. & van Oudenaarden, A. Stochastic gene expression out-of-steady-state in the cyanobacterial circadian clock. *Nature* **450**, 1249–1252 (2007).
15. Kerckhoffs, R. C. P., McCulloch, A., Omens, J. & Mulligan, L. Effects of biventricular pacing and scar size in a computational model of the failing heart with left bundle branch block. *Med. Image Anal.* **13**, 362–369 (2009).
16. Grenier, F., Timofeev, I. & Steriade, M. Neocortical very fast oscillations (ripples, 80–200 Hz) during seizures: intracellular correlates. *J. Neurophysiol.* **89**, 841–852 (2003).
17. Isalan, M. et al. Evolvability and hierarchy in rewired bacterial gene networks. *Nature* **452**, 840–845 (2008).
18. Alon, U. Network motifs: theory and experimental approaches. *Nature Rev. Genet.* **8**, 450–461 (2007).
19. Gibson, D. G. et al. Complete chemical synthesis, assembly, and cloning of a *Mycoplasma genitalium* genome. *Science* **319**, 1215–1220 (2008).
20. Hasty, J., McMillen, D. & Collins, J. J. Engineered gene circuits. *Nature* **420**, 224–230 (2002).
21. Endy, D. Foundations for engineering biology. *Nature* **438**, 449–453 (2005).
22. Gardner, T. S., Cantor, C. R. & Collins, J. J. Construction of a genetic toggle switch in *Escherichia coli*. *Nature* **403**, 339–342 (2000).
23. Elowitz, M. B. & Leibler, S. A synthetic oscillatory network of transcriptional regulators. *Nature* **403**, 335–338 (2000).
24. You, L., Cox, R., Weiss, R. & Arnold, F. Programmed population control by cell–cell communication and regulated killing. *Nature* **428**, 868–871 (2004).
25. Basu, S., Gerchman, Y., Collins, C., Arnold, F. & Weiss, R. A synthetic multicellular system for programmed pattern formation. *Nature* **434**, 1130–1134 (2005).
26. Kobayashi, H. et al. Programmable cells: interfacing natural and engineered gene networks. *Proc. Natl Acad. Sci. USA* **101**, 8414–8419 (2004).
27. Austin, D. W. et al. Gene network shaping of inherent noise spectra. *Nature* **439**, 608–611 (2006).
28. Tabor, J. J. et al. A synthetic genetic edge detection program. *Cell* **137**, 1272–1281 (2009).
29. Friedland, A. E. et al. Synthetic gene networks that count. *Science* **324**, 1199–1202 (2009).
30. Atkinson, M. R., Savageau, M. A., Myers, J. T. & Ninfa, A. J. Development of genetic circuitry exhibiting toggle switch or oscillatory behavior in *Escherichia coli*. *Cell* **113**, 597–607 (2003).
31. Stricker, J. et al. A fast, robust and tunable synthetic gene oscillator. *Nature* **456**, 516–519 (2008).
32. Tigges, M., Marquez-Lago, T., Stelling, J. & Fussenegger, M. A tunable synthetic mammalian oscillator. *Nature* **457**, 309–312 (2009).
33. Fung, E. et al. A synthetic gene-metabolic oscillator. *Nature* **435**, 118–122 (2005).
34. Cookson, N. A., Tsimring, L. S. & Hasty, J. The pedestrian watchmaker: Genetic clocks from engineered oscillations. *FEBS Lett.* **483**, 3931–3937 (2009).
35. Bennett, M. R. & Hasty, J. Microfluidic devices for measuring gene network dynamics in single cells. *Nature Rev. Genet.* **10**, 628–638 (2009).
36. Waters, C. M. & Bassler, B. L. Quorum sensing: cell-to-cell communication in bacteria. *Ann. Rev. Cell Dev. Biol.* **21**, 319–346 (2005).
37. Liu, D. et al. Mechanism of the quorum-quenching lactonase (AiiA) from *Bacillus thuringiensis*. 1. Product-bound structures. *Biochemistry* **47**, 7706–7714 (2008).
38. Glossop, N. R. J., Lyons, L. C. & Hardin, P. E. Interlocked feedback loops within the *Drosophila* circadian oscillator. *Science* **286**, 766–768 (1999).
39. Lakin-Thomas, P. L. & Brody, S. Circadian rhythms in microorganisms: new complexities. *Annu. Rev. Microbiol.* **58**, 489–519 (2004).
40. McMillen, D., Kopell, N., Hasty, J. & Collins, J. Synchronizing genetic relaxation oscillators by intercell signaling. *Proc. Natl Acad. Sci. USA* **99**, 679–684 (2002).
41. Garcia-Ojalvo, J., Elowitz, M. & Strogatz, S. Modeling a synthetic multicellular clock: repressors coupled by quorum sensing. *Proc. Natl Acad. Sci. USA* **101**, 10955–10960 (2004).
42. Reading, N. C. & Sperandio, V. Quorum sensing: the many languages of bacteria. *FEMS Microbiol. Lett.* **254**, 1–11 (2006).
43. Cookson, S., Ostroff, N., Pang, W., Volfson, D. & Hasty, J. Monitoring dynamics of single-cell gene expression over multiple cell cycles. *Mol. Syst. Biol.* **1**, 2005.0024 (2005).
44. Mather, W., Bennett, M., Hasty, J. & Tsimring, L. Delay-induced degrade-and-fire oscillations in small genetic circuits. *Phys. Rev. Lett.* **102**, 068105 (2009).
45. Ozbudak, E. M., Thattai, M., Kurtser, I., Grossman, A. D. & van Oudenaarden, A. Regulation of noise in the expression of a single gene. *Nature Genet.* **31**, 69–73 (2002).
46. Elowitz, M. B., Levine, A. J., Siggia, E. D. & Swain, P. S. Stochastic gene expression in a single cell. *Science* **297**, 1183–1186 (2002).
47. Lutz, R. & Bujard, H. Independent and tight regulation of transcriptional units in *Escherichia coli* via the LacR/O, the TetR/O and AraC/I1–I2 regulatory elements. *Nucleic Acids Res.* **25**, 1203 (1997).
48. Dunlap, P. V. & Greenberg, E. P. Control of *Vibrio fischeri* luminescence gene expression in *Escherichia coli* by cyclic AMP and cyclic AMP receptor protein. *J. Bacteriol.* **164**, 45–50 (1985).
49. Thomas, P. W. et al. The quorum-quenching lactonase from *Bacillus thuringiensis* is a metalloprotein. *Biochemistry* **44**, 7559–7569 (2005).

**Supplementary Information** is linked to the online version of the paper at [www.nature.com/nature](http://www.nature.com/nature).

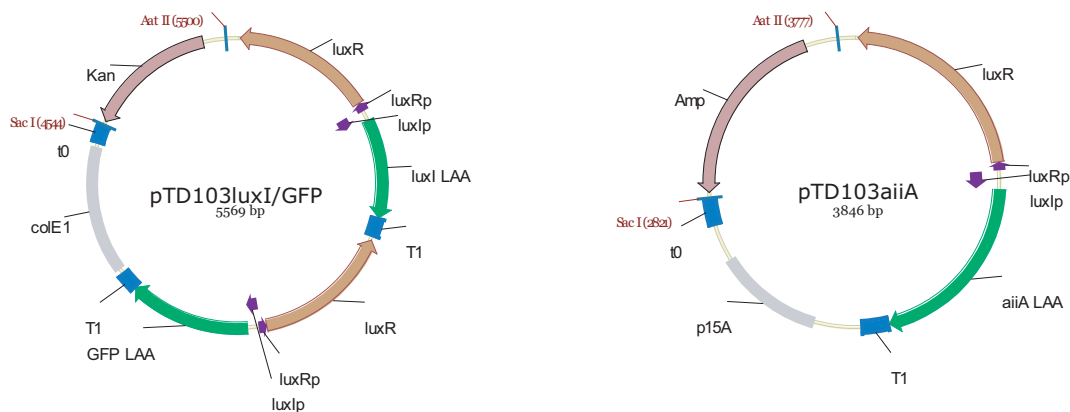
**Acknowledgements** We thank J. Stricker for helpful discussions on plasmid construction, and M. Bennett, K. Wiesenfeld and J. Collins for stimulating discussions during the preparation of the manuscript. This work was supported by the National Institutes of Health and General Medicine (GM69811), the DOE CSGF fellowship (to T.D.), and CONACYT (Mexico, grant 184646, to O.M.-P.).

**Author Contributions** All authors contributed extensively to the work presented in this paper. T.D. and O.M.-P. are equally contributing first authors, and L.T. and J.H. are equally contributing senior authors.

**Author Information** Reprints and permissions information is available at [www.nature.com/reprints](http://www.nature.com/reprints). The authors declare no competing financial interests. Correspondence and requests for materials should be addressed to J.H. ([hasty@bioeng.ucsd.edu](mailto:hasty@bioeng.ucsd.edu)).

## Plasmid Construction

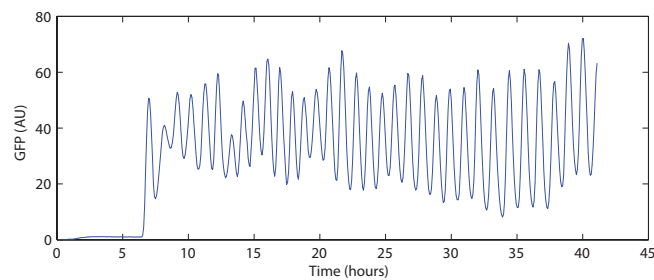
The pTD103 plasmids were constructed by replacing the promoter in a pZ modular plasmid (pZE21yemGFP-LAA) from XhoI to EcoRI restriction sites (Lutz and Bujard (1997)) with the *luxR* gene and the *luxI* promoter amplified via PCR from the native *Vibrio Fischeri* operon (pJE202, Dunlap and Greenberg (1985)). The pZ plasmid RBS was kept the same, and *luxI* or *aiiA* (from pMAL-t-*aiiA*, Thomas et al. (2005)) genes were cloned in place of yemGFP with the TSAAN-DENYALAA degradation tag on the carboxy-terminal (Stricker et al. (2008)). The yemGFP reporter module (*luxR* gene-*luxIp*-yemGFP-LAA) was then amplified with AvrII and NheI restriction sites and ligated into the AvrII site following the terminator in pTD103luxI-LAA.



**Supplementary Figure 1:** Plasmids for the synchronized oscillator strain TDQS1. Construction of the pTD103 plasmids was done in the modular pZ plasmid backbones in three identical transcriptional modules with the same promoter, RBS, and terminator for each.

## Data Analysis

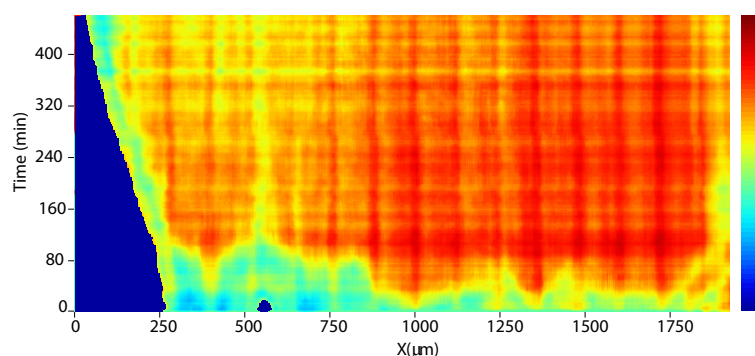
Fluorescence vs. Time curves were obtained by importing fluorescent images into ImageJ and using the 'Intensity vs. Time Monitor' Plug-in to obtain a mean gray value of the entire field of view, and then the background gray value was subtracted (Fig1c 60x magnification, Fig 2a,b 20x magnification). Peak-to-peak values were taken for all period measurements and amplitudes were measured as peak to previous trough values. The data collected in Fig2c,d was obtained from 20x/60x magnification experiments from the parallelized device (Supplement Fig. 3b) in different sized traps. Each data point in Fig. 2c,d represents between 10-40 peak values averaged. We found that traps downstream of each other had similar period/amplitude measurements and including them in our averages did not significantly alter the mean values but greatly reduced the errors bar values. This showed that traps downstream of one another were only weakly coupled at our flow rates. In Suppl Fig2, we plot an additional fluorescence trajectory obtained from imaging one of these traps at 60x showing that oscillations exhibit stably over long periods of time.



**Supplementary Figure 2:** *Stable oscillations in microfluidic device.* Fluorescence vs. Time curve obtained for a 100x84 micron trap over the course of  $\sim 40$  hours.

### Space-Time plots

To create the space-time plot in Fig 3b, we averaged a 20 pixel window along the center of the trap (seen in Fig3a) in fluorescent images. To obtain a semi-quantitative measure of cell density we performed the same process on brightfield images. When no cells were present, the mean gray value was darker due to the lighting on the PDMS (polydimethylsiloxane) device, so we manually corrected the blue region in the bottom left of Suppl. Fig3 where no cells were present. Once cells populated the trap, we found the gray value to give a measure of the density cells (Suppl. Fig3). The periodicity in the data (apparent at high time values) is an artifact from the stitching of images in the Nikon Elements software (due to the slight difference in focal planes when the camera moves). We obtained the space time plot for Fig3d by averaging the fluorescence (20 pixel window) along the center of the colony. We stitched together 3 continuous image sets with image frequencies of 4 minutes (1-45), 3 minutes (frames 46-99) and 2.25 minutes (frames greater than 100). In the displayed images, another colony growing from bottom left begins to merge with the main one, and slightly influences the fluorescent front on the left but did not affect the front to the right.



**Supplementary Figure 3:** *Space-time plot of density of cells in Fig3a experiment.* Gray value of the brightfield images is plotted as a measure of cell density in the 2000x100x0.95 $\mu\text{m}$  device. Red indicates higher cell density.

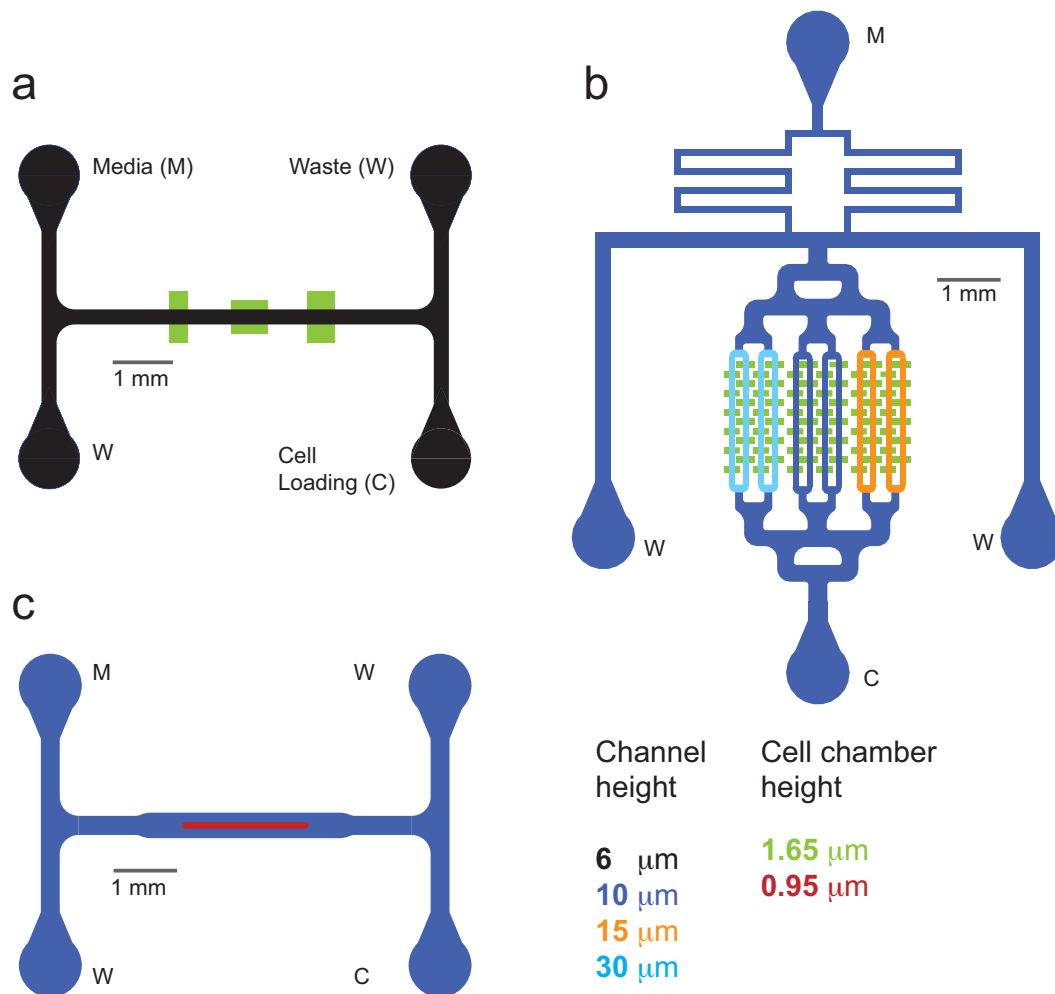
## Microscopy and Microfluidics

A similar microscope setup was used in Stricker et al. (2008), but to maintain temperature at 37°C a plexiglass incubation temperature was used. At 60x, fluorescent images were taken every 3-4.5 minutes which we found to be sufficient to prevent photobleaching (200-500ms exposure, 10% lamp setting). At 20x magnification, fluorescent images could be taken more often (every 2 minutes).

In each device, *E. coli* cells are loaded from the cell port while keeping the media port at sufficiently higher pressure than the waste port below to prevent contamination (Suppl. Fig4). Cells were loaded into the cell traps by manually applying pressure pulses to the lines to induce a momentary flow change. The flow was then reversed and allowed for cells to receive fresh media with 0.075% Tween20 which prevented cells from adhering to the main channels and waste ports. For the yeast device experiments (Fig3c,d), we loaded *E. coli* cells in the main region by not adding surfactant during the loading process.

We initially built the device in Suppl. Fig 4a to test the synchronized oscillator in three different trap sizes with 1.65 $\mu\text{m}$  high trap regions. We found the 1.65 $\mu\text{m}$  height allowed for better growth of cells presumably because of the additional flow of media into the interstitial spaces (as compared to 0.9-1.0 $\mu\text{m}$  high traps). A parallelized version of the chip with 3 channel heights was constructed to generate different flow rates and trap sizes of (70,84,90,100) $\times$ 100  $\mu\text{m}$  (Suppl. Fig3b). We found that the heights of the channels did not greatly affect the period measurements presumably since the relevant parameter is only the flow rate in the plane of the trap, and this did not significantly differ between channel heights. Thus, to alter the flow rates we increased the heights of the media reservoir to create different flow rates. To estimate flow rates, we measured the length of traces of fluorescent beads (1.0  $\mu\text{m}$ ) upon 100ms exposure to fluorescent light to establish a measure for the average velocity of as a function of height of the media reservoir. We averaged over at least 1000 data points for each to obtain the average velocities in Fig.2c (x-axis), which confirmed that the velocity scales linearly with the pressure difference caused by the height of the media reservoir.

To study spatial temporal behavior of the synchronized oscillator, we designed a microfluidic trap that is 20 times as long (2mm) and 100  $\mu\text{m}$  wide as the original traps (Suppl. Fig4c). Unlike the traps in Suppl. Fig 4a,b, the trap is only 0.95  $\mu\text{m}$  high and we found this height optimal for seeding cells in the trap. Since the trap lacks any walls it is open to the flow, it would be difficult to seed cells in a non constraining device. Given the open boundary conditions and the constriction of rod-shaped *E. coli* bacteria to one layer, cells arrange parallel to each other and perpendicular to the edges of the trap. This ordering leads to a very tight packing of a monolayer of cells. Under these conditions, the transport of nutrients, AHL and cell waste happen mainly by diffusion and is less sensitive (but not insensitive) to the flow rate of surrounding media than in the cell traps of devices *a* and *b* below. An example of this is that bursts of fluorescence propagate in both directions of the trap irrespective of the sense of external flow at very high flow rates. In the experiment shown in Suppl. Movie 3, the flow rate was set close to 100  $\mu\text{m}/\text{s}$  to counter the increased adherence of cells after long run times, which we believe might be caused by growing them in media with surfactant Tween 20 after long durations.



**Supplementary Figure 4:** Microfluidic Devices constructed for this study. *a*) Device used initially to test the TDSQ1 cells for synchronized oscillations. The dimensions of the traps from left to right are  $100 \times 100 \mu\text{m}$ ,  $200 \times 50 \mu\text{m}$  and  $150 \times 100 \mu\text{m}$ , respectively. Traps scaled 300% in this schematic for visualization. *b*) Parallelized version of Device *a*. Several trap sizes and channel heights could be tested simultaneously. Traps are  $100 \mu\text{m}$  wide and either 70, 84, 90, or  $100 \mu\text{m}$  deep. *c*) Device used for the wave propagation experiments in Fig 3a,b in the main text. The trap is  $2000 \times 100 \mu\text{m}$  wide.

## Modeling

There has been much work on modeling asynchronous, oscillating cells coming into synchrony in the context of synthetic biology (McMillen et al. (2002); Garcia-Ojalvo et al. (2004)), though less attention has been focused on gene networks that do not oscillate in individual cells but oscillate collectively (Ma and Yoshikawa (2009)). Here we constructed a deterministic model of quorum-sensing gene clock. From the biochemical reactions depicted in Fig. 1a, we derived the following set of delay-differential equation model for intracellular concentrations of LuxI ( $I$ ), AiiA ( $A$ ), internal AHL ( $H_i$ ), and external AHL ( $H_e$ ),

$$\frac{\partial A}{\partial t} = C_A[1 - (d/d_0)^4] P(\alpha, \tau) - \frac{\gamma_A A}{1 + f(A + I)} \quad (1)$$

$$\frac{\partial I}{\partial t} = C_I[1 - (d/d_0)^4] P(\alpha, \tau) - \frac{\gamma_I I}{1 + f(A + I)} \quad (2)$$

$$\frac{\partial H_i}{\partial t} = \frac{bI}{1 + kI} - \frac{\gamma_H A H_i}{1 + gA} + D(H_e - H_i) \quad (3)$$

$$\frac{\partial H_e}{\partial t} = -\frac{d}{1-d} D(H_e - H_i) - \mu H_e + D_1 \frac{\partial^2 H_e}{\partial x^2} \quad (4)$$

We did not include an equation for LuxR assuming that it is constitutively produced at a constant level. Previous work found that LuxR is under control of the LuxR-AHL complex to produce a higher concentration of LuxR but we did not find this necessary to capture the essential behavior of the synchronized oscillator (Williams et al. (2008)).

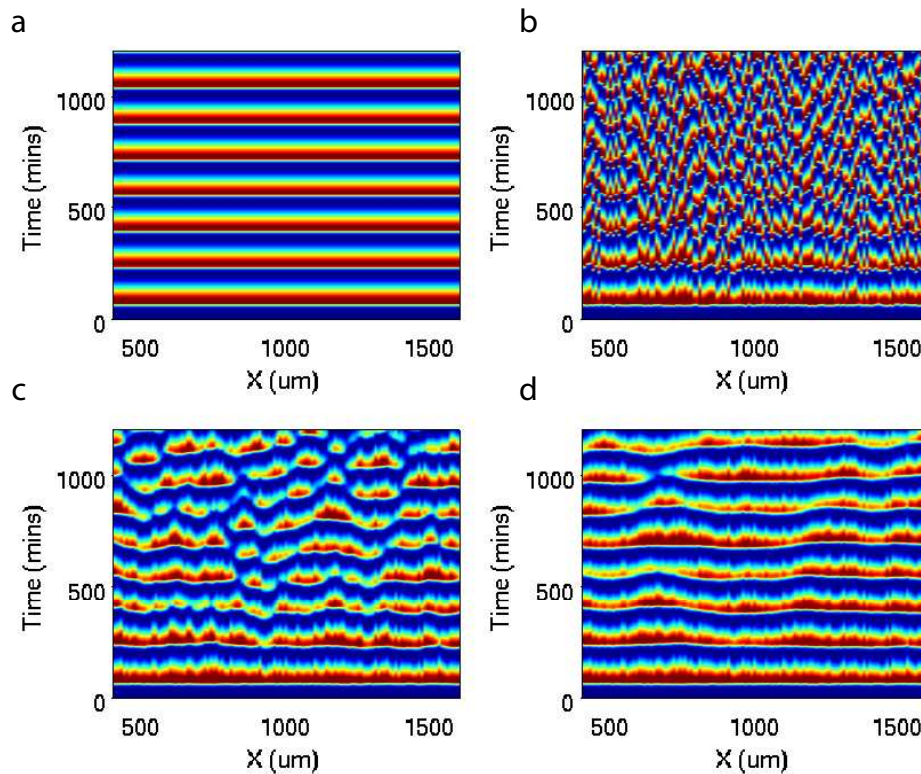
In the first two equations, the Hill function

$$P(\alpha, \tau) = \frac{\delta + \alpha H_\tau^2}{1 + k_1 H_\tau^2}$$

describes the delayed production of corresponding proteins, it depends on the past concentration of the internal AHL,  $H_\tau(t) = H_i(t - \tau)$ . These delayed reactions mimic the complex cascades of processes (transcription, translation, maturation, etc.) leading to formation of functional proteins. The pre-factor  $[1 - (d/d_0)^4]$  describes slowing down of protein synthesis at high cell density  $d$  due to lower nutrient supply and high waste concentration. Terms proportional to  $\gamma_x$  describe enzymatic degradation of proteins and AHL by proteases inside of the cell due to their degradation tags. We model these processes using Michaelis-Menten kinetics. Terms proportional to  $D$  describe diffusion of AHL through cell membrane, and the term proportional to  $\mu$  models dilution of external AHL by external fluid flow. The cell density ( $d$ ) determines the amount of external AHL and thus affects the AHL decay rate. The factor  $d/(1-d)$  follows from the total mass conservation of AHL inside and outside the cells. Since the flow speed ( $\sim 100\mu\text{m}/\text{sec}$ ) is much higher than the typical wave propagation speed ( $\sim 10\mu\text{m}/\text{sec}$ ), we neglected the anisotropy imposed by the fluid flow. The last term in equation for  $H_e$  describes the diffusion of external AHL.

We used the following experimentally relevant scaled parameters in most of our simulations:  $C_A = 1, C_I = 4, \delta = 10^{-3}, \alpha = 2500, \tau = 10, k = 1, k_1 = 0.1, b = 0.06, \gamma_A = 15, \gamma_I =$

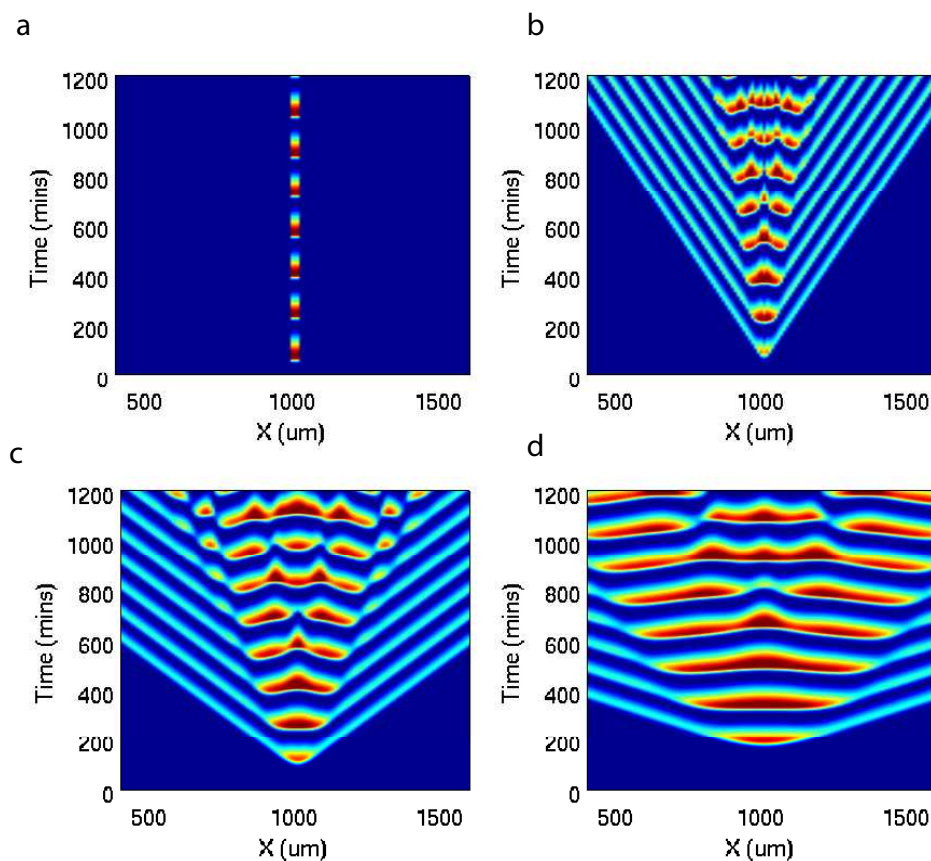
24,  $\gamma_H = 0.01$ ,  $f = 0.3$ ,  $g = 0.01$ ,  $d_0 = 0.88$ ,  $D = 2.5$ . We varied the diffusion constant  $D_1$  and the external AHL decay rate (flow rate)  $\mu$ , as well as the cell density  $d$ . For “bulk” simulations we dropped the diffusion term  $\sim D_1$  in equation for  $H_e$ , and solved the resulting set of ordinary delay-differential equations. For spatio-temporal simulations we replaced the partial delay-differential equations by a one-dimensional array of  $N = 200$  systems of ordinary delay-differential equations representing individual “cells” coupled via a second-order discrete diffusion operator  $D_1 dx^{-2}[H_{i-1} + H_{i+1} - 2H_i]$  for the external AHL concentration. We used periodic boundary conditions at the ends of the array ( $H_1 = H_N$ ).



**Supplementary Figure 5:** Synchronization of oscillations in spatially extended system with diffusion. The parameters ( $p$ ) of each of 200 oscillators were varied around their nominal values ( $p_0$ ) as  $p = p_0(1 + \eta\zeta)$  where  $\zeta$  is a random number uniformly distributed between -0.5 and 0.5, and  $\eta$  characterizes the fluctuations magnitude. To illustrate the role of spatial diffusion in mitigating the stochastic fluctuations, we varied  $\eta$  and  $D_1$ : a,  $\eta = 0$ ,  $D_1 = 0$ , b,  $\eta = 0.1$ ,  $D_1 = 0$ , c,  $\eta = 0.1$ ,  $D_1 = 800\mu\text{m}^2/\text{sec}$ , d,  $\eta = 0.1$ ,  $D_1 = 4000\mu\text{m}^2/\text{sec}$ ,

In addition to the numerical results presented in the Main Text, we show here the results of additional spatiotemporal simulations. In particular, Suppl. Fig. 5 shows the synchronization of oscillations in cell population with statistically different parameters. As seen from the figure, the coherence of oscillations increases with the diffusion coefficient  $D_1$ , as expected. In Suppl. Fig. 6 we show the propagation of waves initiated by a localized initial condition ( $I_{N/2} = 1$  while all other  $I_i = 0$  and  $A_i = 0$ ) for different diffusion constants. Since parameter  $\delta$  characterizing the leakiness of the *luxI* promoter is small ( $10^{-3}$ ), the basal state with  $A = I = 0$  is very weakly unstable. Thus, in the absence of AHL diffusion ( $D_1 = 0$ ), while the middle cell begins to

oscillate immediately, all other cells are still quiescent (Suppl. Fig. 5a). However, when the diffusion is present ( $D_1 \neq 0$ ), cells influence their neighbours and oscillations propagate in the form of traveling waves in both directions (Suppl. Fig. 6b-d). As seen from this set of space-time diagrams, the wave speed increases with  $D_1$ . Fig. 4d of the Main text shows that this dependence is well approximated by the formula  $V \approx 0.17d_1^{1/2}\mu\text{m}/\text{sec}$ .



**Supplementary Figure 6:** Wave propagation in the spatially uniform system with different external AHL diffusion rates: a,  $D_1 = 0$ , b,  $D_1 = 200\mu\text{m}^2/\text{sec}$ , c,  $D_1 = 800\mu\text{m}^2/\text{sec}$ , d,  $D_1 = 4000\mu\text{m}^2/\text{sec}$ ,

## References

- Dunlap, P. and Greenberg, E. (1985). Control of *Vibrio fischeri* luminescence gene expression in *Escherichia coli* by cyclic AMP and cyclic AMP receptor protein. *Journal of bacteriology* 164:45–50.
- Garcia-Ojalvo, J., Elowitz, M. and Strogatz, S. (2004). Modeling a synthetic multicellular clock: Repressilators coupled by quorum sensing. *Proceedings of the National Academy of Sciences* 101:10955–10960.
- Lutz, R. and Bujard, H. (1997). Independent and tight regulation of transcriptional units in *Escherichia coli* via the LacR/O, the TetR/O and AraC/I1-I2 regulatory elements. *Nucleic acids research* 25:1203.
- Ma, Y. and Yoshikawa, K. (2009). Self-sustained collective oscillation generated in an array of nonoscillatory cells. *Physical Review E* 79:46217.
- McMillen, D., Kopell, N., Hasty, J. and Collins, J. (2002). Synchronizing genetic relaxation oscillators by intercell signaling. *Proceedings of the National Academy of Sciences* 99:679–684.
- Stricker, J., Cookson, S., Bennett, M., Mather, W., Tsimring, L. and Hasty, J. (2008). A fast, robust and tunable synthetic gene oscillator. *Nature* 456:516–519.
- Thomas, P., Stone, E., Costello, A., Tierney, D., Fast, W. et al. (2005). The quorum-quenching lactonase from *Bacillus thuringiensis* is a metalloprotein. *Biochemistry(Washington)* 44:7559–7569.
- Williams, J., Cui, X., Levchenko, A. and Stevens, A. (2008). Robust and sensitive control of a quorum-sensing circuit by two interlocked feedback loops .

## Supplementary Movies

Supplementary Movie 1. Timelapse fluorescence microscopy of TDQS1 cells at low flow rate in a  $100 \times 100 \mu\text{m}$  trap. Fluorescence is shown in cyan hot color table (dark blue low, white high). Total time of movie is 483 min with a sampling rate of one image every 3 min.

Supplementary Movie 2. Timelapse fluorescence microscopy of TDQS1 cells in a  $2000 \times 100 \times 0.95 \mu\text{m}$  open trap showing propagation of AHL at millimeter scale. The brightfield image is shown in gray, and fluorescence is shown in cyan hot color table (dark blue low, white high). Total time of movie is 962 min with a sampling rate of one image every 3 min.

Supplementary Movie 3. Timelapse microscopy of TDQS1 cells at high flow rate in a  $100 \times 100 \mu\text{m}$  trap. Fluorescence is shown in cyan hot color table (dark blue low, white high). Total time of movie is 867 min with a sampling rate of one image every 3 min.

Supplementary Movie 4. Zoomed timelapse fluorescence microscopy of TDQS1 cells in a  $2000 \times 100 \times 0.95 \mu\text{m}$  open trap showing close-up of cells and propagation of AHL. The brightfield image is shown in gray, and fluorescence is shown in cyan hot color table (dark blue low, white high). Total time of movie is 962 min with a sampling rate of one image every 3 min.

Supplementary Movie 5. Timelapse fluorescence microscopy of TDQS1 cells in a three dimensional  $1000 \times 400 \times 4.0 \mu\text{m}$  trap. The brightfield image is shown in gray, and fluorescence is shown in cyan hot color table (dark blue low, white high). Total time of movie is 636 min with a sampling rate of one image every 2.25-4 min.

Supplementary Movie 6. Simulation of the wave propagation within a uniform population of cells. The oscillations are initiated by a small perturbation in the middle of the chamber. The space-time diagram corresponding to this simulation is shown in Fig. 4e of the Main text.

Supplementary Movie 7. Simulation of the wave propagation within a growing dense cluster of cells. The oscillations are initiated by a small perturbation in the middle of the initially small cluster. The space-time diagram corresponding to this simulation is shown in Fig. 4f of the Main text.